Accurate Coronary Centerline Extraction, Caliber Estimation, and Catheter Detection in Angiographies

Antonio Hernández-Vela, Carlo Gatta, Sergio Escalera, Laura Igual, Victoria Martín-Yuste, Manel Sabaté, and Petia Radeva

***Abstract*—Segmentation of coronary arteries in X-ray angiography is a fundamental tool to evaluate arterial diseases and choose proper coronary treatment. The accurate segmentation of coronary arteries has become an important topic for the registration of different modalities, which allows physicians rapid access to different medical imaging information from computed tomography (CT) scans or magnetic resonance imaging (MRI). In this paper, we propose an accurate fully automatic algorithm based on Graph-cuts for vessel centerline extraction, caliber estimation, and catheter detection. Vesselness, geodesic paths, and a new multiscale edgeness map are combined to customize the Graph-cuts approach to the segmentation of tubular structures, by means of a global optimization of the Graph-cuts energy function. Moreover, a novel supervised learning methodology that integrates local and contextual information is proposed for automatic catheter detection. We evaluate the method performance on three datasets coming from different imaging systems. The method performs as good as the expert observer with respect to centerline detection and caliber estimation. Moreover, the method discriminates between arteries and catheter with an accuracy of 96.5%, sensitivity of 72%, and precision of 97.4%.**

***Index Terms*—Angiography, caliber, catheter, centerline (CL), Graph-cuts (GC), quantitative coronary angiography (QCA), segmentation, X-Ray.**

I. Introduction

QUANTITATIVE coronary angiography (QCA) tools are used by clinicians on daily basis to evaluate the degree of coronary lesions and proceed with the proper intervention. Automatic enhancement and segmentation of vessel structures has become a basic tool to assist clinicians for a more accurate, fast, and objective patient data analysis. The main aim of this multimodal registration, especially between X-ray and computed tomography (CT), is to retrieve the 3-D shape of the artery from the CT data, having a 2-D projection and estimate the most probable 3-D deformation, as pointed out in several papers [1]–[4]. Furthermore, multimodal registration allows rapid access to complementary information about the coronary tree and its lesions coming, e.g., from CT scans or other imaging modalities. However, vessel segmentation in angiography sequences is still challenging; highly reliable, fully automatic methods are not established yet.

In this paper, we use Graph-cuts (GC) theory [5]–[8] to model vessel structures and obtain a globally optimal segmentation of the coronary tree in angiography images, achieving accurate detection of both the centerline and the vessel borders. One of the critical issues for GC is the design of proper energy terms to assure optimal analysis of local image structures and global segmentation solution. In particular, the original GC definition suffers from the shrinking bias drawback [9] since it tends to produce small contours corresponding to the minimal cut. Hence, with the original GC energy formulation, it is not well suited to segment tubular structures and thin objects like blood vessels. Moreover, X-ray images are characterized by low signal-to-noise ratio, subtle vessel appearance, vessel bifurcation, crossing ambiguity, and variable image contrast.

In this study, we propose a novel GC energy functional tailored to the vessel segmentation problem. The novel energy formulation takes into account 1) the local vessel appearance, using a vesselness measure; 2) the local connectivity to other vessel regions, using geodesic paths; and 3) a measure of edgeness based on a new multiscale version of the adaptive Canny detector [10], which allows an accurate vessel boundary detection. In order to discriminate the catheter guide (from now on, we will refer to the catheter guide as "catheter," for compactness) from vessels, we define a set of appearance features and propose a supervised learning approach based on the multiscale stacked sequential learning. Finally, we propose three datasets, which allow the quantitative evaluation of the method. A preliminary study of this paper was published in [11]. In this paper, we introduce the following novelties with respect to the previous medical image computing and computer assisted intervention (MICCAI) paper: 1) a new method for catheter detection, which completes the methodology of coronary centerline (CL) extraction, caliber estimation, and catheter detection in angiographies, from a technological and clinical point of view; 2) an extended dataset: more images have been added to DS1, and a new DS3 dataset has been introduced to show the robustness of the method proposed; and 3) a complete evaluation framework is presented, including new and more detailed experiments, performance measures, and discussions of the results.

Manuscript received January 12, 2012; revised May 26, 2012, August 2, 2012, and September 14, 2012; accepted September 16, 2012. Date of current version November 16, 2012. This work was supported in part by the Project La Marató de TV3 082131, Project TIN2009-14404-C02, and Project CONSOLIDER-INGENIO CSD 2007-00018. The work of C. Gatta was supported by a "Beatriude Pinos" grant and by a "Ramon y Cajal" contract. The work of A. Hernandez-Vela was supported by an Formación de Personal Universitario fellowship from the Spanish government.

A. Hernández, C. Gatta, S. Escalera, L. Igual, and P. Radeva are with the Department of Matemàtica Aplicada i Anàlisis, Universitat de Barcelona, Gran Via de les Corts Catalanes 585, 08007 Barcelona, Spain, and also with the Computer Vision Center, Campus Universitat Autònoma de Barcelona, Edifici O, 08193 Barcelona, Spain (e-mail: ahernandez@cvc.uab.es; carlo.gatta@cvc.uab.es; sescalera@cvc.uab.es; ligual@cvc.uab.es; petia@cvc.uab.es).

V. Martín-Yuste and M. Sabaté are with the Institut Clínic del Tòrax, Hospital Clínic de Barcelona, Villarroel, 08036 Barcelona, Spain (e-mail: 27700vmy@comb.cat; msabate@clinic.ub.es).

Color versions of one or more of the figures in this paper are available online at http://ieeexplore.ieee.org.

Digital Object Identifier 10.1109/TITB.2012.2220781

The rest of this paper is organized as follows. Section II presents an overview of the state-of-the-art and related work, Section III provides background concepts used in our method, Section IV presents our proposal, and Section V explains the validation protocol used to obtain the results, which are commented in Section VI. Finally, Section VII contains the discussion, and Section VIII concludes this paper.

II. Related Work

Several methods that exploit photometric and structural properties of tubular structures have been proposed so far [12]–[16]. An excellent review of basic geometrical features for tubular-like structures can be found in [17]. Nonetheless, in the case of vessel segmentation in angiography sequences, the problem is still challenging; highly reliable, fully automatic methods are not established yet [18]. Moreover, the accurate vessel caliber estimation is still a hot topic far from being solved, as demonstrated by the scale selection method proposed in [19]. An extensive overview of different methods for vessel extraction can be found in [20]. Recently, an interesting approach to vessel segmentation has been proposed in [21], which fuses local features with local directional information; unfortunately, the authors do not provide a quantitative evaluation of their method. In [19], the authors propose a method for scale selection that improves the caliber estimation, and show results on the retinal DRIVE dataset [22] and synthetic images.

Nonetheless, most works are based on local image analysis to extract vessels or employ an *a priori* model to help vessel extraction. In contrast, the GC technique is an optimal segmentation tool that combines local and contextual image information analysis by modeling relations between neighboring pixels [6], [7], [23]. The goodness of the GC solution depends on the suitability of the energy terms and their reliable computation. It is worth to mention that GC suffers from the "shrinking bias" problem; since the energy function definition makes it proportional to the length of the boundary of the result, GC is biased to segment small, isotropic regions. This problem can be overcome in different ways. Works like [9] and [24] have addressed this problem by incorporating flux information in the GC framework. In [25], the authors include a geodesic distance term to the GC energy function, computed from some strokes manually defined by the user as an initialization step of the segmentation. Differently than previous methods, we tailor the GC energy function in such a way that long and thin structures can be easily and automatically segmented. To the best of our knowledge none of the previous methods incorporates local appearance, geodesic paths, and an edgeness measure in a compact, unified framework.

III. Background

In this section, we overview the GC framework and the vesselness measure, which are employed in our method.

A. Graph-Cuts

Let us define $\mathcal{X} = (\mathbf{x}_1, \ldots, \mathbf{x}_i, \ldots, \mathbf{x}_{|\mathcal{P}|})$ the set of pixels for a given grayscale image I; $\mathcal{P} = (1, \ldots, i, \ldots, |\mathcal{P}|)$ the set of indexes of I; $\mathcal{N}$ the set of unordered pairs $\{i, j\}$ of neighboring pixels of $\mathcal{P}$ under a $4-$ $(8-)$ neighborhood system, and $L = (L_1, \ldots, L_i, \ldots, L_{|\mathcal{P}|})$ a binary vector whose components L_i specify assignments to pixels $i \in \mathcal{P}$. Each L_i can be either "fore" or "back" indicating if it belongs to the foreground or background, respectively. GC formulation [7] defines the cost function $E(L)$, which describes soft constraints imposed on boundary and region properties of L as

$$E(L) = U(L) + \lambda B(L) \tag{1}$$

the unary term is denoted as

$$U(L) = \sum_{i \in \mathcal{P}} U_i(L_i) \tag{2}$$

and the boundary term as

$$B(L) = \sum_{\{i,j\} \in \mathcal{N}} B_{\{i,j\}}\, \Omega(L_i, L_j) \tag{3}$$

where the characteristic function $\Omega(L_i, L_j)$ is 0 if $L_i = L_j$ and 1, otherwise. The unary term $U(L)$ is defined assuming that individual penalties for assigning pixel i to "fore" and "back" [i.e., $U_i(\text{fore})$ and $U_i(\text{back})$] are given by foreground and background models. In our case, the foreground is the vessel denoted by "vess." The term $B(L)$ comprises the boundary properties of segmentation L. Any $B_{\{i,j\}} \geq 0$ should be interpreted as a penalty for a discontinuity between i and j. Finally, the coefficient $\lambda \in \mathbb{R}^+$ specifies the relative importance of the boundary term against the unary term. The GC algorithm imposes hard constraints on the segmentation result by means of the definition of seed points where labels are predefined and cannot be modified. The notations $\mathcal{V} \subset \mathcal{P}, \mathcal{B} \subset \mathcal{P}, \mathcal{V} \cap \mathcal{B} = \emptyset$ refer to the subsets of vessel (our foreground object of interest) and background seeds, respectively. Boykov and Funka-Lea [7] show how to efficiently compute the global minimum of $E(L)$ among all segmentations L satisfying the hard constraints $\forall i \in \mathcal{V}, L_i =$ "vess," $\forall i \in \mathcal{B}, L_i =$ ''back,'' using a minimum cut algorithm on a graph defined by nodes and edges, which are image pixels and pixel relations, respectively. Let us describe the details of the graph created to segment an image. A graph $\mathcal{G} = \langle \Upsilon, \mathcal{E} \rangle$ is created with nodes Υ corresponding to pixels $i \in \mathcal{P}$ of the image. There are two additional nodes: the foreground terminal (source S) and the background terminal (sink T); therefore, $\Upsilon = \mathcal{P} \cup \{S, T\}$. The set of edges $\mathcal{E}$ consists of two types of undirected edges: n-links (neighborhood links) and t-links (terminal links). Each pixel i has two t-links $\{i, S\}$ and $\{i, T\}$ connecting it to each terminal. Each pair of neighboring pixels $\{i, j\}$ in $\mathcal{N}$ is connected by an n-link. Without introducing any ambiguity, an n-link connecting a pair of neighbors i and j will be denoted by $\{i, j\}$, giving

$$\mathcal{E} = \mathcal{N} \bigcup_{i \in \mathcal{P}} \{\{i, S\}, \{i, T\}\}. \tag{4}$$

Graph $\mathcal{G}$ is completely defined when assigning weights to the edges in the way described in Table I, where $K = 1 + \max_{i \in \mathcal{P}} \sum_{j:\{i,j\} \in \mathcal{N}} B_{\{i,j\}}$.

TABLE I
WEIGHTS OF EDGES IN $\mathcal{E}$

edge	weight (cost)	for
$\{i,j\}$	$B_{\{i,j\}}$	$\{i,j\} \in \mathcal{N}$
$\{i,S\}$	$U_i(\text{“}back\text{”})$	$i \in \mathcal{P}, i \notin \mathcal{V} \cup \mathcal{B}$
	K	$i \in \mathcal{V}$
	0	$i \in \mathcal{B}$
$\{i,T\}$	$U_i(\text{“}vess\text{”})$	$i \in \mathcal{P}, i \notin \mathcal{V} \cup \mathcal{B}$
	0	$i \in \mathcal{V}$
	K	$i \in \mathcal{B}$

B. Vesselness

The vesselness measure $V(i,s)$ is computed as follows [26]:

$$V(i,s) = \begin{cases} 0, & \text{if } \lambda_2(i,s) > 0 \\ e^{-\frac{\mathcal{R}_B{}^2(i,s)}{2b^2}} \left(1 - e^{-\frac{\mathcal{S}^2(i,s)}{2c^2}}\right), & \text{otherwise.} \end{cases} \tag{5}$$

Two measures are used: a geometric ratio based on the second-order ellipsoid which accounts for the deviation from a blob-like structure $\mathcal{R}_B(i,s) = |\lambda_1(i,s)|/\sqrt{|\lambda_2(i,s)|}$, and the second-order structuredness $\mathcal{S}(i,s) = \sqrt{\sum_{j=1,2} \lambda_j^2(i,s)}$, where $\lambda_1(i,s)$ and $\lambda_2(i,s)$ ($|\lambda_1| \leq |\lambda_2|$) are the eigenvalues of the Hessian matrix of image I computed at scale s and location i. Parameters b and c control the sensitivity of the filter to the measures $\mathcal{R}_B$ and $\mathcal{S}$.

Differential operators involved in the Hessian computation are well-posed concepts of linear scale-space theory, defined as convolutions with derivatives of Gaussians

$$\frac{\partial}{\partial i} I(\mathbf{i}, s) = s^{\ell} I(i) * \frac{\partial}{\partial i} G(\mathbf{i}, s) \tag{6}$$

where G is the 2-D Gaussian function and ℓ is the Lindeberg parameter.

Given Q different possible scales, i.e., $s \in \{s^{(1)}, \ldots, s^{(Q)}\}$, (5) can be evaluated at each of the Q scales. In [26], the authors estimate the vesselness V at every pixel i as $V(i) = \max_{s \in \{s^{(1)}, \ldots, s^{(Q)}\}} V(i,s)$.

IV. METHOD

In this section, we present a fully automatic method for vessel segmentation based on GC theory.

A. Seed Initialization

In order to achieve a fully automatic methodology, we exploit the inherent structure of vessels to define vessel seeds—-as the foreground object—based on valleys, and background seeds based on low probabilities of the vesselness image [26]. In particular, vessel seeds $\mathcal{V}$ correspond to those pixels corresponding to the highest responses on a multilocal valley detector (multilocal refers to the case where more than one ridge are connected, in a drainage pattern) with structure tensor, namely $\mathcal{S}_t$, as described in [27]

$$\mathcal{V} = \{i | \mathcal{S}_{t,i} > \Theta_v\} \tag{7}$$

where $\mathcal{S}_{t,i}$ is the valley response at pixel i, and Θ_v is a sensitivity valley threshold.

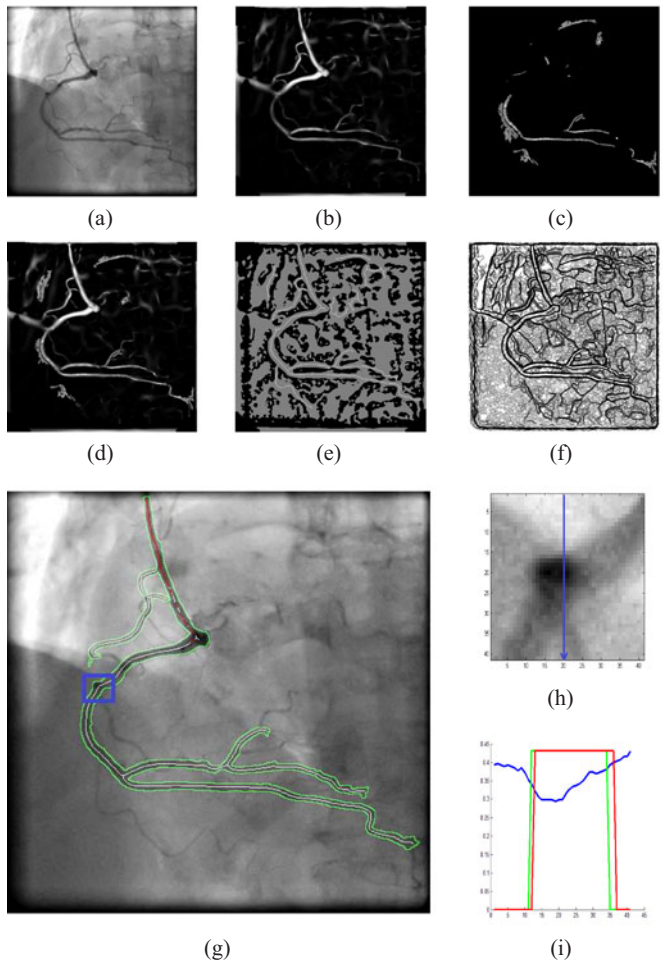

Fig. 1. Method: (a) input image, (b) Frangi vesselness map, (c) geodesic map, (d) unary potential: vesselness-geodesic map, (e) vessel-background seeds (in white and black), (f) boundary potential: multiscale edgeness map (darker values correspond to higher J_i^*), (g) final segmentation, centerline estimation, and catheter detection (in green, white, and red, respectively), (h) zoomed ROI corresponding to blue rectangle in (g), (i) in blue: vessel intensity variation along the blue line in (h); in red: ground-truth segmentation; in green: our segmentation.

The background seeds $\mathcal{B}$ are the pixels corresponding to low probabilities in the vesselness image $V(i)$:

$$\mathcal{B} = \{i | V(i) \leq \Theta_b\} \tag{8}$$

where Θ_b is a sensitivity vesselness threshold and $V(i)$ the vesselness measure at pixel i. Fig. 1(e) shows the selection of $\mathcal{V}$ and $\mathcal{B}$ seeds for the input image in Fig. 1(a).

B. Unary Term

We define the vessel and background models combining the vesselness map $V(i)$ and the geodesic distance map D_i. Vesselness provides us the probability of tubular structures; however, some vessel regions can have low vessel probabilities. To avoid this problem, we exploit geodesic paths among vessel seeds and use geodesic distance in the definition of a new vesselness-geodesic measure VG. Let us first introduce the computation of geodesic paths and geodesic distance map necessary to define VG.

Geodesic distance map: intuitively, the geodesic distance map contains the distances of each pixel to a set of centroids of a k-means clustering over the Cartesian coordinates of the vessel seeds.

From the set $\mathcal{C}_{\{i,j\}}$ of all possible paths between points i and j, we select the one with minimum distance:

$$\Gamma^*_{\{i,j\}} = \underset{\Gamma \in \mathcal{C}_{\{i,j\}}}{\operatorname{argmin}} D(\Gamma) \tag{9}$$

where $\Gamma = \{i, \ldots, j\}$ is an arbitrary parametrized discrete path defined by $|\Gamma| = R$ pixels, and $D(\Gamma)$ is the geodesic distance of Γ defined as

$$D(\Gamma) = m(\|\nabla I(\Gamma)\|^2) \left(\sum_{i=1}^{R-1} \frac{\|\nabla I_i\|^2}{R} \right) \tag{10}$$

where the quantity $\|\nabla I_i\|$ is a finite difference approximation of the image gradient between points $(\mathbf{x}_i, \mathbf{x}_{i+1})$, and the function $m(\mathbf{z})$ represents the maximum difference of the R-dimensional vector $\mathbf{z}$, so that

$$m(\mathbf{z}) = \max_{i,j \in \Gamma} |\mathbf{z}_i - \mathbf{z}_j|. \tag{11}$$

The distance D, as defined in (10), is normalized by the length R of the path to make the measure independent of the path length. Moreover, the distance is penalized by the maximum difference $m(\mathbf{z})$ of image gradients within the path to control the gradient variations and avoid abrupt changes.

The path $\Gamma^*_{\{i,j\}}$ is computed incrementally using a standard Dijkstra-like short-path algorithm. After computing the partial path $\Gamma^*_{\{i,q\}}$, in order to select the next path point $q^* \in \mathcal{N}_q$, where $\mathcal{N}_q$ is the set of 8-neighbor of q, we use the following criterion:

$$q^* = \underset{\ell \in \mathcal{N}_q}{\operatorname{argmin}} (D(\Gamma^*_{\{i,q\}}) + \sigma_{\{q,\ell\}} D(\Gamma_{\{q,\ell\}})) \tag{12}$$

where $\sigma_{\{q,\ell\}}$ is the Euclidean distance between the Cartesian coordinates of pixels q and ℓ. Once the next point has been selected, we continue the path only if $D(\Gamma^*_{\{i,q^*\}}) < \Theta_d$, where Θ_d is an X-ray dependent empirically set threshold. Since different geodesic maps can be found for different initialization pixels j, the geodesic distance map, for each pixel i, is computed as

$$D_i = \min_j D(\Gamma^*_{\{j,i\}}). \tag{13}$$

These pixels j are the centroids of a k-means clustering over the Cartesian coordinates of the vessel seeds. In other words, the initialization pixels j are used as the starting points for the computation of the paths $\Gamma^*_{j,i}$, until $D(\Gamma^*_{\{i,q^*\}}) \geq \Theta_d$. Through the iterations of the algorithm for each initialization point j, several pixels are supposed to be visited. Therefore, every pixel i is supposed to be visited at least once, for any of the initialization pixels. Finally, when computing the final geodesic distance map D_i, costs obtained from each initialization point are merged using the minimum operator.

In particular, the map VG for pixel i is computed as the maximum between the vesselness value and the normalized "inverse" of the geodesic distance

$$VG_i = \max \left(V(i), \ \frac{\frac{1}{D_i + \mu(D)}}{\max(\frac{1}{D + \mu(D)})} \right) \tag{14}$$

where D and $\mu(D)$ correspond to the geodesic distance map and its mean, respectively.

We initialize the unary potentials at each pixel i as

$$U_i(\text{“vess”}) = -\ln(p(L_i = \text{“vess”})) \tag{15}$$

$$U_i(\text{“back”}) = -\ln(p(L_i = \text{“back)}). \tag{16}$$

The probability of a pixel to be marked as "vess" is computed using the vesselness-geodesic measure $VG, p(L_i = \text{“vess”}) = VG(\mathbf{x}_i)$ and the opposite probability as $p(L_i = \text{“back”}) = 1 - p(L_i = \text{“vess”})$. An example of the VG map is shown in Fig. 1(d).

C. Boundary Term

We propose an image-dependent multiscale edgeness measure. First, we run the Canny edge detector algorithm on the image at different threshold levels. Then, we compute the edge probability at each pixel by averaging the edge thresholds for different scales as follows:

$$J^*_i = \min_j \frac{1}{n} \sum_{e=1}^{n} J_{i,\Theta_e,s^j} \tag{17}$$

where J_{i,Θ_e,s^j} is the binary edge map using the threshold Θ_e and scale s^j for pixel i. If pixel i is labeled as an edge pixel for most of the threshold levels at a significant scale, it has a high probability of being an edge pixel. The final boundary potential over the multiscale edgeness map is computed as $B_{\{i,j\}} = J^*_i$. An example of J^*_i is shown in Fig. 1(f).

D. Graph-Cuts Segmentation

Finally, we apply the min-cut [23] algorithm in order to find the segmentation with the minimum energy. Then, once we obtain the segmentation from GC, we keep only the biggest connected component in the final segmentation. An example of the final segmentation is shown in green in Fig. 1(g).

E. Centerline Extraction and Caliber Estimation

The CL is computed as follows: given the binary segmentation L, we compute its distance map $M(L)$. Then, a nonmaxima suppression is applied to find local maxima and a classic ridge transversal method is applied to connect the local maxima. The ridge transversal stops when it finds another CL or it exits the segmented area. Fig. 1(g) shows an example of an extracted CL in white. Vessel caliber is estimated by applying a local Laplacian of Gaussian (LoG) filtering at CL locations at different scales. The scale space computed using $\sigma^2 \text{LoG}(x, y; \sigma)$ has a minimum at $\sigma = w/2$, where w is the width of the ridge.

F. Catheter Detection

By merely its appearance, the catheter is not easily distinguishable from arteries. In order to discriminate between vessels and catheter, we propose a classification method based on suitable catheter features, where every CL path is considered as a 1-D object in the 2-D image plane. The algorithm is based on the multiscale stacked sequential learning [28], which is divided into two steps: first, a pointwise classification method is

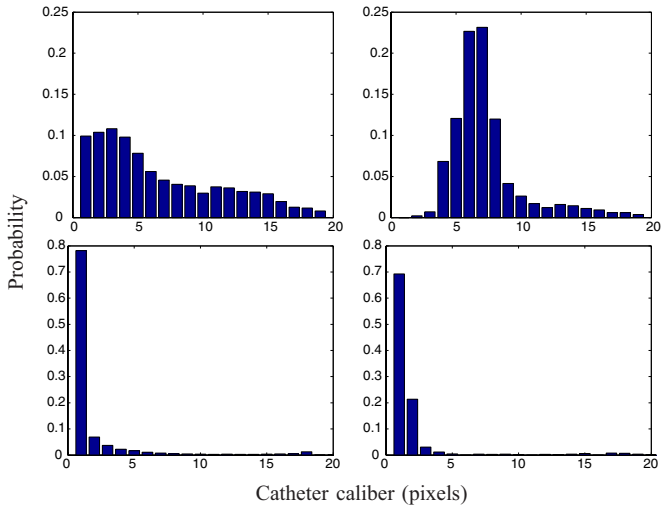

Fig. 2. First row: artery (left) and catheter (right) caliber distribution, in pixels. x-axis represents the catheter caliber and y-axis represents the corresponding probability of the histogram bins. Second row: artery (left) and catheter (right) caliber variation distribution.

performed using an Adaboost classifier with decision stumps, and second, contextual information is extracted and used as input for another classifier, in order to refine the previous results using contextual information. For each point of the CL path, we extract five features.

1) *Position* $\mathbf{x} = (x, y)$: Configuration of catheter and artery in angiography can be learned by our method.
2) *Curvature*: In order to accurately compute the curvature, we fit a cubic spline to the CL curve [29]. We approximate the curvature at subpixel resolution by computing $x'y'' - y'x''/(x'^2 + y'^2)^{3/2}$.
3) *Angular direction*: We take advantage of the spline representation to compute the angular direction at point $\mathbf{x}$ as $\tan y'/x'$.
4) *Caliber*: Although the segmentation results provide the caliber estimation, we use vesselness measures [26] to describe caliber feature, since we can similarly compute it in training and test stages.
5) *Caliber first-order derivative*: Finally, caliber variation is useful to discriminate between catheter and artery.

Fig. 2 shows the difference of distribution for artery and catheter caliber computed on a set of 20 angiography images (first row) and the caliber variation on artery and catheter (second row). In Fig. 3 the results of both steps of the catheter detection are shown. The result of the pointwise classifier is displayed on the right-upper image. On the right-lower image, it can be seen that misclassified pixels are correctly classified by means of the stacked classifier.

V. Experiments

In order to present the results, we describe the material, methods, and validation protocol of the experiments.

A. Material

We defined three datasets, named DS1, DS2, and DS3. DS1 is formed by 20 images from ten patients, acquired with a single

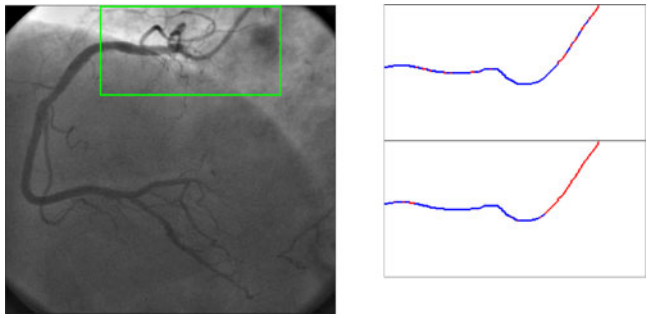

Fig. 3. Catheter detection example. On the right-upper image, the result of the pointwise Adaboost classifier is shown. The right-lower image corresponds to the result of the stacked classifier. Vessel and catheter are represented in green and red, respectively.

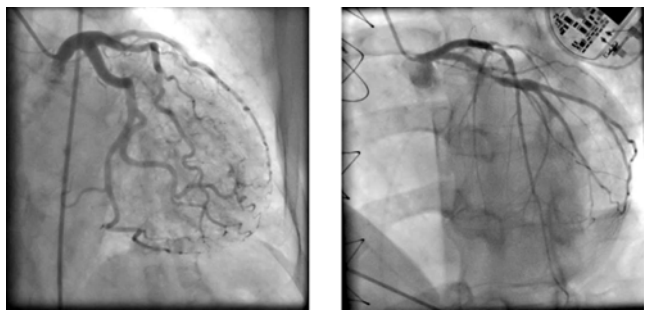

(a) (b)

Fig. 4. Example dataset images from (a) DS2 and (b) DS3 .

plane Philips INTEGRIS Allura Flat Detector, of Right Coronary Arteries (RCA). Three experts have blindly annotated—i.e., without seeing the annotations from other experts—all the visible CLs of the artery tree. The experts also annotated the CLs with different labels: "vess," the arteries that potentially can present a clinical interest, i.e., with a caliber of at least 1 mm; "don't care," all other arteries in the image, which are too small to be of clinical interest; and "cat," the catheter guide. This dataset has been mainly designed to perform the algorithm tuning, the evaluation of CL extraction and catheter detection.

The dataset DS2 is formed by 31 images from 27 patients, acquired with a SIEMENS Artis zee, of 10 RCAs, 10 left anterior descending arteries (LAD), and 11 circumflex coronary arteries (Cx). Two experts blindly segmented a total of 41 lesions (12 LADs, 13 Cxs, and 16 RCAs) assisted by a semiautomatic method (QCA-CMS Version 6.0, MEVIS, Bremen, Germany). The experts were asked to manually correct unsatisfactory segmentations. The required time for the semiautomatic segmentation plus manual correction of incorrect segmentations is 26.6 ± 17 and 26.3 ± 15 s for observer 1 and 2, respectively. The images in this dataset present relatively easy cases in which the degree of the stenosis is not relevant. Moreover, the only structure that can make the segmentation difficult is the diaphragm: the diaphragm boundary can disturb the correct identification of vessels boundary, and it could also reduce the image contrast locally. Fig. 4(a) shows an example image from DS2.

The third dataset (DS3) has been thought as a highly challenging set of images, with the aim of creating a dataset that fosters the research on automatic vessel segmentation in complex X-ray

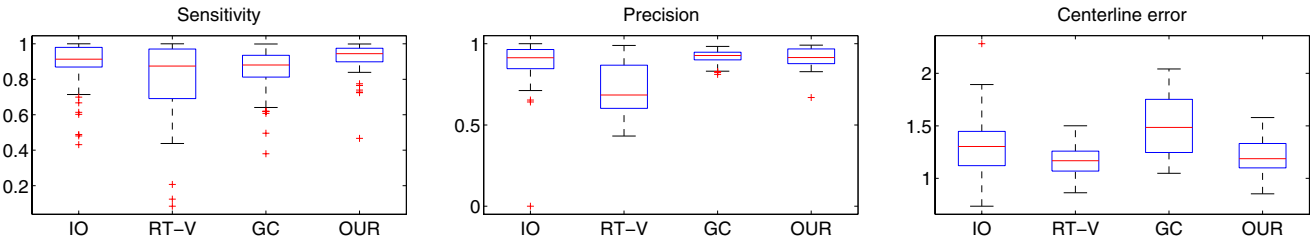

Fig. 5. Centerline evaluation results for DS1: sensitivity (left), precision (middle), and centerline error (right).

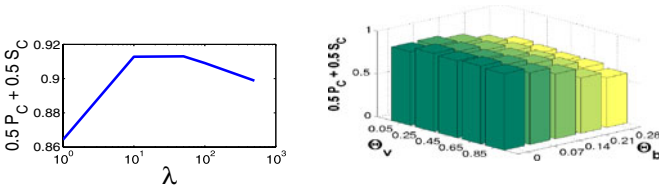

(a) (b)

Fig. 6. Systematic parameter study. The performance of the system is analyzed for different values of the following parameters: (a) GC boundary potential weight λ and (b) sensitivity vesselness thresholds Θ_v and Θ_b.

angiographies. All the images have been acquired with patients presenting diffused lesions, from real cases of daily clinical practice. The image can present one or more of the following characteristics: severe stenosis, tri-vascular stenosis, stent(s), sternal wires, pacemaker, pacing wires, and reduced artery staining. This dataset is formed by 40 images from 23 patients, acquired with a SIEMENS Artis zee, of 17 RCAs, 15 LADs, and 8 Cxs. Two experts blindly segmented a total of 48 lesions (19 LADs, 9 Cxs, and 20 RCAs) assisted by a semiautomatic method (QCA-CMS Version 6.0, MEVIS). The experts were asked to manually correct unsatisfactory segmentations. The required time for the semiautomatic segmentation plus manual correction of incorrect segmentations is 39.7 ± 17 and 32.5 ± 29 s for observer 1 and 2, respectively. It is interesting to note that, on average, the time required for the segmentation for the DS3 is more than the one required for the DS2 (about 10 s), showing that the images present much more complicated structures, requiring more manual correction. Fig. 4(b) shows an example image from DS3, where sternal wires and the pacemaker are visible.

B. Methods

We compare our proposed method against a classic ridge transversal CL extraction method applied to the Frangi vesselness result (RT-V), and the GC method without our proposed geodesic distance in the unary potential, and the multiscale edgeness map in the boundary potential. Furthermore, we also compare the obtained results with the interobserver (IO) variability of the experts ground truth (GT). In the case of the proposed method and GC, parameters Θ_v, Θ_b, and λ are tuned via cross-validation over DS1. Given N patients, the tuning is performed using a leave one patient out (LOPO) methodology by maximizing $0.5P_c + 0.5S_c$ in order to provide a balance between precision P_c and sensitivity S_c. Fig. 6 shows the effect of these three parameters on the performance of the proposed method. On one hand, Fig. 6(a) shows the performance for different values of the boundary potential weight λ (here Θ_v and Θ_b are fixed). On the other hand, Fig. 6(b) shows the effect of the vesselness thresholds Θ_b and Θ_v on the final result (λ is fixed in this plot). Having a look at these plots, we see that Θ_b has an important influence on the final result. In contrast, λ and Θ_v do not seem to be as critical as Θ_b, although the correct tuning of them raises the performance metric by 5% in the best case. In all experiments $s = \{0.81, 1.09, \ldots, 2.46\}$ mm, $b = 0.75$, $c = 0.33$, $\Theta_d = 0.05$, $\Theta_e \in [0.02, 0.03, \ldots, 0.3]$, $s^j \in [0.5, 1, \ldots, 5]$, and pixels $k = 10$.

C. Validation Protocol

We propose to validate the output of our proposed method on three main aspects: 1) centerline; 2) caliber; and 3) catheter.

1) Centerline: to evaluate the CL detection, we computed the precision P_c, sensitivity S_c, and the localization error $\mathcal{E}_L$. To compute P_c and S_c, we define a threshold Θ_c, which defines the maximal distance between the ground truth CL and the detected CL. To calculate the S_c, we check for every CL point in the GT if there exists a detected CL point in a distance smaller than Θ_c; if this happens, this point is considered as a true positive (TP). Similarly, P_c is computed by checking for each detected CL point if there exists a GT CL in a neighborhood of radius Θ_c. The localization error $\mathcal{E}_L$ is then computed as the distance between the points in the detected CL and the nearest point in the GT, as long as this distance is lower than Θ_c. The parameter Θ_c has been experimentally set to 5 pixels to allow large localization $\mathcal{E}_L$ errors. Precision, sensitivity, and the localization error $\mathcal{E}_L$ have been computed on DS1.

2) Caliber: using the segmentation provided by the observers over DS2 and DS3, we approximate two cubic splines to each segmented artery boundaries. Using these splines, we determine the CL and extract the caliber for each CL location [19]. For each point in the GT CL, we identify the nearest point in the detected CL and evaluate the caliber estimation error with two measures: we compute the signed error $\Delta D_c = D_c - D_c^*$ and its absolute value, where D_c^* is the ground truth caliber in millimeters.

3) Catheter: catheter detection has been evaluated with standard machine learning performance measures: accuracy, sensitivity, specificity, and precision. Quantitative evaluation is performed on the dataset DS1, for which observers provided reliable GT. Examples of catheter detection are evaluated in a qualitative way on images from DS2 and DS3.

VI. Results

We divide the results into CL, caliber, and catheter estimation evaluation.

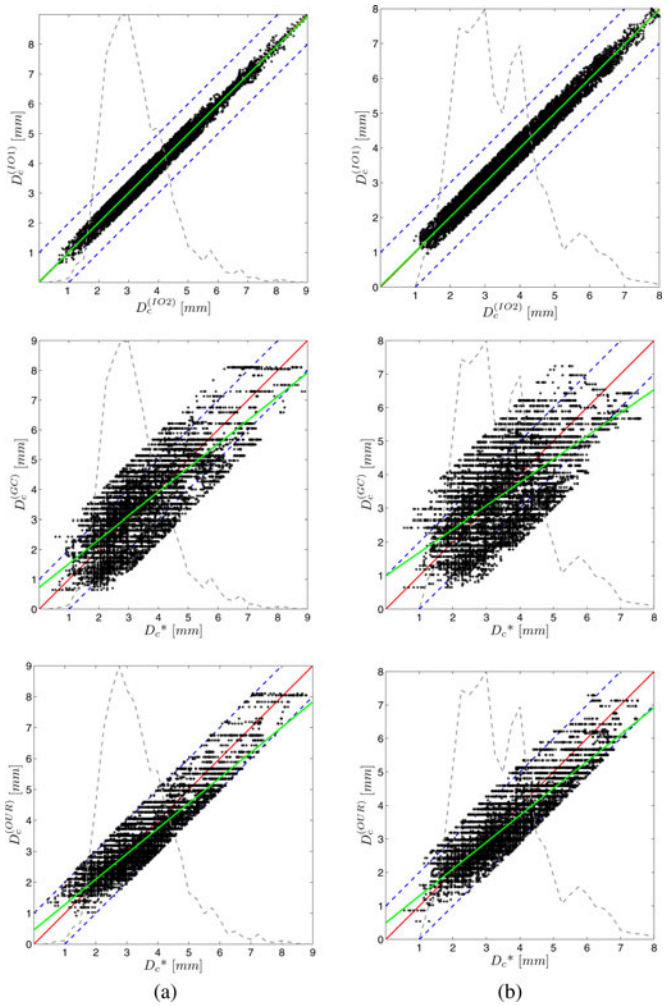

Fig. 7. GT and estimated calibers in scatter plots for IO variability (first row), GC (second row), and our method (third row) in (a) DS2 and (b) DS3.

A. Centerline Evaluation

Fig. 5 shows S_c, P_c, and $\mathcal{E}_L$ for the IO variability, the RT-V, GC, and the proposed method for the dataset DS1[1]. The RT-V method has the lowest S_c and a very low P_c, while the $\mathcal{E}_L$ is extremely low; this confirms that the vesselness measure is well suited to accurately detect the CL, but it has the disadvantage to produce many FPs as confirmed by the low P_c, and false Negatives (FN) as shown by S_c. A basic GC approach increases both S_c and P_c, while $\mathcal{E}_L$ is increased due to inaccurate border detection using a gray-level-based boundary term. Our proposed method shows the highest S_c and P_c, and a $\mathcal{E}_L$ that is very close to RT-V, while actually detecting more vessel pixels than both RT-V and GC (higher S_c, less false negatives). It is also interesting to note that the proposed method has a lower P_c than the IO variability but higher S_c; this means that the proposed method still produces some FPs but tends to detect clinically relevant arteries in a way that is the "average" of the observers.

[1]The results are available at www.cvc.uab.es/∼ahernandez/AccCentExtr.zip.

TABLE II
CALIBER ESTIMATION QUANTITATIVE RESULTS (IN MILLIMETERS)

	DS2		DS3	
	$\lvert\Delta D_c\rvert$	ΔD_c	$\lvert\Delta D_c\rvert$	ΔD_c
IO	0.18 ± 0.24	-0.001 ± 0.3	0.18 ± 0.21	0.005 ± 0.28
GC	0.84 ± 0.74	0.096 ± 1.12	1.02 ± 0.85	0.005 ± 1.33
Ours	0.49 ± 0.55	-0.1 ± 0.73	0.56 ± 0.61	-0.13 ± 0.82

TABLE III
SEPARATE QUANTITATIVE RESULTS ON DS2 AND DS3: LAD, RCA, AND CX

	LAD	RCA	CX
DS2	0.57 ± 0.64	0.42 ± 0.43	0.52 ± 0.62
DS3	0.56 ± 0.62	0.55 ± 0.59	0.59 ± 0.71

TABLE IV
PERFORMANCE OF THE POINTWISE ADABOOST AND THE MR-SSL CLASSIFICATION FOR CATHETER DETECTION

	Adaboost	MR-SSL
Accuracy	0.9250	0.9456*
Sensitivity	0.4009	0.5191*
Specificity	0.9750	0.9863
Precision	0.9446	0.9555

The asterisk denotes that the null hypothesis can be rejected at the 5% level, using the t-test, when comparing Adaboost to MR-SSL.

B. Caliber Evaluation

Fig. 7 shows scatter plots of the caliber estimation on datasets DS2 and DS3 for the IO variability, the basic GC, and the proposed method, respectively. The gray-dashed curve shows the density of points w.r.t. the caliber. The basic GC method performs badly, as confirmed by the large absolute error of 0.84 ± 0.74 mm in DS2, and 1.02 ± 0.85 mm in DS3 (see Table II), while the proposed method performs much better having an average absolute error of 0.49 ± 0.55 mm and 0.56 ± 0.61 in DS2 and DS3, respectively. Table III shows the caliber estimation error of our proposed method on DS2 and DS3 separated by the type of artery; as expected, the error is lower for the RCAs. Furthermore, Table II shows the average signed error, which gives an estimate of the method bias. It is worth to note that for humans the two datasets are equally easy to segment, given the very low interobserver variability both in absolute term and bias. The proposed method has a little negative bias on both datasets and provides, as expected, a smaller absolute error for the dataset DS2. The error increment from DS2 to DS3 is lower for our algorithm w.r.t. GC.

C. Catheter Evaluation

Table IV shows the result of catheter detection in terms of accuracy, sensitivity, specificity, and precision. Results are separated showing the performance of a pointwise Adaboost classification, and the advantage of the use of a context-aware classifier. To visually appreciate the advantage of using Multiscale Multiresolution Stacked Sequential Learning (MR-SSL), Fig. 3 shows an example of catheter classification; the scattered classification produced by the pointwise Adaboost is polished by the contextual part of the MR-SSL. Moreover, Fig. 8 shows two qualitative results of catheter detection.

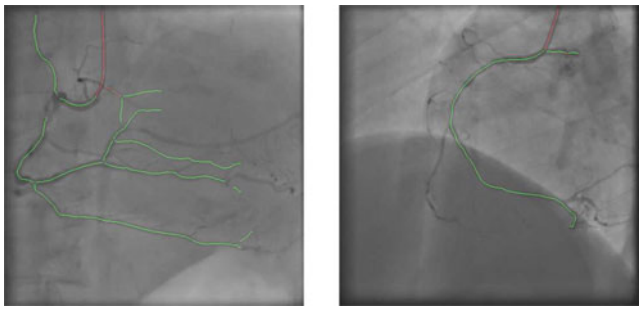

Fig. 8. Qualitative results for catheter detection in DS2. Pixels detected as catheter are shown in red; the rest of the centerline is shown in green.

VII. Discussion

The main goal of this study is to exploit the power of the Graph-cuts method while, at the same time, solve the most relevant problems in accurate vessel segmentation. We tailored GC to the specific goal, facing several issues. Vesselness-like measures perform poorly in the proximity of bifurcations; the proposed unary potential, thanks to the geodesic component, allows us to mitigate this problem, providing connected CLs at bifurcation locations. The proposed boundary term, thanks to the novel multiscale edgeness measure, allows the segmentation to stop at vessel boundaries. Fig. 1(h) clearly shows the ability of the proposed method in a complicated gray-level local distribution. Another important property of the proposed method is its accuracy in the CL detection. The proposed catheter detection method exploits the power of machine learning approaches that also considers the neighbor labeling results to improve the classification. We believe this approach is far more general than the one proposed in [21]. Nonetheless, there are several issues that could be addressed. In many cases, the contrast liquid flux that moves back in the aorta can be confused with a thick, low contrasted, artery. Artery overlapping, especially for LAD, can result in incorrect segmentation in which the caliber is overestimated or bifurcations are erroneously detected.

It is finally worth to mention that, while in segmentation problems, generally, the direct measure of segmentation accuracy is preferred, in the segmentation of arteries the most important thing is to properly detect the CL and its caliber. Relying on observer pixel-wise segmentation could be dangerous since there is a large interobserver variability on which arteries should be segmented and which can be safely omitted. This claim is confirmed by the IO statistics in Fig. 5. While the IO precision is very high, the sensitivity can be significantly low even using our "indirect" measure. A direct measurement would show even lower figures for the interobserver variability, which do not correspond to the observer ability in defining the CL and the artery boundary, as confirmed by the low interobserver error in both Fig. 5 (slightly above 1 pixel) and Tables II and III (almost no bias and just 0.18 mm average interobserver error).

Regarding the complexity of the algorithm, the computational cost of the proposed method is $O(|\mathcal{P}| + \frac{|\mathcal{N}|}{|\mathcal{P}|}\log|\mathcal{P}|)$, the GC algorithm is $O(|\mathcal{E}||\mathcal{P}||\mathcal{C}|)$, where C is the cost of the minimum cut, and the geodesic computation is $O(|\mathcal{P}| + \frac{|\mathcal{N}|}{|\mathcal{P}|}\log|\mathcal{P}|)$. In terms of absolute time consuming, the MATLAB code of the whole procedure on a conventional two-core computer of 2.6 GHz and 8 GB spends an average of 20 s per image.

VIII. Conclusion

We presented a novel segmentation method for X-ray angiography images that takes into account vessel appearance, artery tree continuity, and borders appearance within Graph-cuts. The algorithm has been tested on three new datasets. Despite being tuned on DS1, the proposed method provided excellent results on DS2 and good results on DS3, showing the inherent robustness of the approach. Future lines of research encompass the use of a high-order potential to deal with irregularity at bifurcations and crossings, a supervised method to optimize the seed selection, and a method to segment overlapped arteries based on contrast liquid opacity.

References

[1] H. Sundar, A. Khamene, C. Xu, F. Sauer, and C. Davatzikos, "A novel 2-D–3-D registration algorithm for aligning fluoro images with 3D pre-op CT/MR images," in *Proc. SPIE—Med. Imag.*, 2006, vol. 6141, pp. 760–766.

[2] C. T. Metz, M. Schaap, S. Klein, L. A. Neefjes, E. Capuano, C. Schultz, R. J. Geuns, P. W. Serruys, T. Walsum, and W. J. Niessen, "Patient specific 4D coronary models from ECG-gated CTA data for intra-operative dynamic alignment of CTA with X-ray images," *Med. Image Comput. Comput. Assist. Interv.*, vol. 12, pp. 369–376, 2009.

[3] C. T. Metz, M. Schaap, S. Klein, A. C. Weustink, N. R. Mollet, C. Schultz, R. J. Van Geuns, P. W. Serruys, T. Van Walsum, and W. J. Niessen, "GPU accelerated alignment of 3-D CTA with 2-D X-ray data for improved guidance in coronary interventions," in *Proc. IEEE Int. Symp. Biomed. Imag*, 2009, pp. 959–962.

[4] E. Serradell, A. Romero, R. Leta, C. Gatta, and F. Moreno-Noguer, "Simultaneous correspondence and non-rigid 3D reconstruction of the coronary tree from single X-ray images," in *Proc. Int. Conf. Comput. Vis.*, 2011, pp. 850–857.

[5] Y. Y. Boykov and M.-P. Jolly, "Interactive graph cuts for optimal boundary & region segmentation of objects in N-D images," in *Proc. Int. Conf. Comput. Vis.*, 2001, vol. 1, pp. 105–112.

[6] Y. Boykov and V. Kolmogorov, "An experimental comparison of min-cut/max-flow algorithms for energy minimization in vision," in *Proc. Int. Conf. Pattern Anal. Mach. Intell.*, 2004, vol. 26, pp. 359–374.

[7] Y. Boykov and G. Funka-Lea, "Graph cuts and efficient N-D image segmentation," *Int. J. Comput. Vis.*, vol. 70, no. 2, pp. 109–131, 2006.

[8] C. Rother, V. Kolmogorov, and A. Blake, "Grabcut: Interactive foreground extraction using iterated graph cuts," *J. ACM Trans. Graph.*, vol. 23, no. 3, pp. 309–314, 2004.

[9] V. Kolmogorov and Y. Boykov, "What metrics can be approximated by geo-cuts, or global optimization of length/area and flux," in *Proc. Int. Conf. Comput. Vis.*, 2005, vol. 1, pp. 564–571.

[10] S. Candemir and Y. Akgul, "Adaptive regularization parameter for graph cut segmentation," in *Image Analysis and Recognition*. New York: Springer, 2010, pp. 117–126.

[11] A. Hernández-Vela, C. Gatta, S. Escalera, L. Igual, V. Martin-Yuste, and P. Radeva, "Accurate and robust fully-automatic QCA: method and numerical validation," *Med. Image Comput. Comput. Assist. Interv.*, vol. 14, pp. 496–503, 2011.

[12] M. Schaap *et al.*, "Standardized evaluation methodology and reference database for evaluating coronary artery centerline extraction algorithms," *Med. Image Anal.*, vol. 13, no. 5, pp. 701–14, 2009.

[13] F. Benmansour and L. Cohen, "Tubular structure segmentation based on minimal path method and anisotropic enhancement," *Int. J. Comput. Vis.*, vol. 92, pp. 192–210, 2011.

[14] D. Lesage, E. D. Angelini, I. Bloch, and G. Funka-Lea, "A review of 3D vessel lumen segmentation techniques: Models, features and extraction schemes," *Med. Image Anal.*, vol. 13, no. 6, pp. 819–845, 2009.

[15] N. Sang, H. Li, W. Peng, and T. Zhang, "Knowledge-based adaptive thresholding segmentation of digital subtraction angiography images," *Image Vis. Comput.*, vol. 25, no. 8, pp. 1263–1270, Aug. 2007.

[16] D. Franchi, P. Gallo, L. Marsili, and G. Placidi, "A shape-based segmentation algorithm for x-ray digital subtraction angiography images," *Comput. Methods Prog. Biomed.*, vol. 94, no. 3, pp. 267–278, Jun. 2009.
[17] K. Krissian, G. Malandain, N. Ayache, R. Vaillant, and Y. Trousset, "Model-based detection of tubular structures in 3d images," *Comput. Vis. Image Understand.*, vol. 80, no. 2, pp. 130–171, 2000.
[18] P. Fallavollita and F. Cheriet, "Towards an automatic coronary artery segmentation algorithm," in *Proc. Eng. Med. Biol. Soc.*, 2006, pp. 3037–3040.
[19] H. Mirzaalian and G. Hamarneh, "Vessel scale-selection using MRF optimization," in *Proc. IEEE Conf. Comput. Vis. Pattern Recog.*, Jun. 2010, pp. 3273–3279.
[20] C. Kirbas and F. Quek, "A review of vessel extraction techniques and algorithms," *ACM Comput. Surv.*, vol. 36, no. 2, pp. 81–121, 2004.
[21] M. Schneider and H. Sundar, "Automatic global vessel segmentation and catheter removal using local geometry information and vector field integration," in *Proc. IEEE Int. Symp. Biomed. Imag*. Piscataway, NJ: IEEE Press, 2010, pp. 45–48.
[22] J. Staal, M. D. Abràmoff, M. Niemeijer, M. A. Viergever, and B. van Ginneken, "Ridge-based vessel segmentation in color images of the retina," *IEEE Trans. Med. Imag.*, vol. 23, no. 4, pp. 501–509, Apr. 2004.
[23] V. Kolmogorov and R. Zabih, "What energy functions can be minimized via graph cuts," *IEEE Trans. Pattern Anal. Mach. Intell.*, vol. 26, no. 2, pp. 147–159, 2004.
[24] A. Vasilevskiy and K. Siddiqi, "Flux maximizing geometric flows," *IEEE Trans. Pattern Anal. Mach. Intell.*, vol. 24, no. 12, pp. 1565–1578, Dec. 2002.
[25] B. L. Price, B. Morse, and S. Cohen, "Geodesic graph cut for interactive image segmentation," in *Proc. IEEE Trans. Comput. Vis. Pattern Recog.*, 2010, pp. 3161–3168.
[26] R. F. Frangi, W. J. Niessen, K. L. Vincken, and M. A. Viergever, "Multiscale vessel enhancement filtering," in *Medical Image Computing and Computer-Assisted Intervention*, (Lecture Notes Computer Science, Vol. 1496). New York: Springer-Verlag, 1998, pp. 130–137.
[27] A. M. Lopez, F. Lumbreras, J. Serrat, and J. J. Villanueva, "Evaluation of methods for ridge and valley detection," in *Proc. Int. Conf. Pattern Anal. Mach. intell.*, 1999, vol. 21, pp. 327–335.
[28] C. Gatta, E. Puertas, and O. Pujol, "Multi-scale stacked sequential learning," *Pattern Recognit.*, vol. 44, no. 10–11, pp. 2414–2426, 2011.
[29] C. de Boor, *A Practical Guide to Splines*. New York: Springer-Verlag, 1978.

Antonio Hernández-Vela received the B.S. degree in computer science and the M.S. degree in computer vision and artificial intelligence, both from the Universitat Autnoma de Barcelona (UAB), Barcelona, Spain, in 2009 and 2010, respectively, where he is currently working toward the P.h.D. degree in mathematics on human pose recovery and behavior analysis.

He is a Research Member at the Computer Vision Center, UAB, and a member of the BCN Perceptual Computing Lab, which is a consolidated research group of Catalonia. His main research interests include the application of computer vision and artificial intelligence to projects that can help impaired people to improve their quality, specially in the field of human pose recovery and behavior analysis.

Carlo Gatta received the M.S. degree in electronic engineering in 2001 from the Università degli Studi di Brescia, Brescia, Italy. In 2006, he received the Ph.D. degree in computer science from the Università degli Studi di Milano, Milan, Italy, with a thesis on perceptually based color image processing.

In September 2007, he joined the Computer Vision Center, Universitat Automona de Barcelona, Barcelona, Spain, as a Postdoctoral Researcher involving mainly in medical imaging. He is member of the Computer Vision Center and the BCN Perceptual Computing Lab. He is currently a Senior Researcher at the Computer Vision Center, under the Ramon y Cajal program. His main research interests include image processing, medical imaging, computer vision, machine learning, and contextual learning.

Sergio Escalera received the B.S. degree in computer science and the M.S. degrees in computer vision and artificial intelligence, both from the Universitat Autónoma de Barcelona (UAB), Barcelona, Spain, in 2003 and 2005, respectively. He received the P.h.D. degree on multiclass visual categorization systems at Computer Vision Center, UAB, where he received the 2008 Best Thesis Award in computer science .

He is a Lecturer in the Department of Applied Mathematics and Analysis, UAB. He is a part-time Professor at Universitat Oberta de Catalunya. He is a member of the Perceptual Computing Group and a consolidated research group of Catalonia. He is also a member of the Computer Vision Center at Campus UAB and International Foundation of Research and Analysis. His research interests include, between others, machine learning, statistical pattern recognition, visual object recognition, and human computer interaction systems, with special interest in human pose recovery, and behavior analysis

Dr. Escalera is an Editorial Board Member of *Journal of Convergence Section C: Web and Multimedia, WebmedCentral, WebmedCentral Plus, American Journal of Intelligent Systems, and Journal of Advanced Computer Science and Technology*.

Laura Igual received the B.S. degree in mathematics from Universitat de Valencia, Valencia, Spain, in 2000. She studied at Université de Liège, Liege, Belgium for a year. She developed her Ph.D. Thesis in computer science and digital communication from the Department of Technology, the Universitat Pompeu Fabra, Barcelona, Spain, partially supported by the French Centre National d'Etudes Spatiales (CNES), Paris, and the company THALES, Neuilly-sur-Seine, France. She received the Ph.D degree in January 2006.

Since 2006, she has been a Research Member at the Computer Vision Center, Universitat Autnoma de Barcelona, Barcelona. She is currently a Lecturer in the Department of Mathematics, Universitat de Barcelona. She is a member of the Perceptual Computing Group and a consolidated research group of Catalonia. Her research interest includes medical imaging.

Victoria Martín-Yuste, photograph and biography not available at the time of publication.

Manel Sabaté received the B.S. degree in Medicine from the Central University of Barcelona, Barcelona, Spain, in June 1990. In December 1995, he graduated Cardiologist after residency training stage of Cardiology (1990–1995) in the Hospital Princeps d'Espanya in Bellvitge, Barcelona. He received the Ph.D. degree (cum laude) from Erasmus University, Rotterdam Holland, in 2000.

From October 1997 to October 1999, he joined the Catheterization Laboratory, Thoraxcenter, Rotterdam, the Netherlands, under the supervision of Dr. Patrick W. Serruys. From October 1999 until July 2005, he was an Interventional Cardiologist in the Interventional Cardiology Department, Hospital Clinico San Carlos, Madrid, Spain. From July 2005 until September 2009, he served as Head of the Interventional Cardiology Unit of the Hospital de la Santa Creu i Sant Pau, Barcelona. He is currently the Head of Cardiology Department of Hospital Clinic, Barcelona.

Petia Radeva received the Ph.D. degree in computer science from the Universitat Autònoma de Barcelona (UAB), Barcelona, Spain. Her Ph.D. dissertation was focused on the development of physics-based models applied to image analysis.

She is currently a Researcher with the Computer Vision Center, UAB. She is also currently an Associate Professor with the Department of Applied Mathematics and Analysis, Universitat de Barcelona. Her research interests include the development of physics-based and statistical approaches for object recognition, medical image analysis, and industrial vision.